A novel approach for determination of nucleation rates and interfacial energy of metallic magnesium nanoclusters at high temperature using non-isothermal TGA models

Prachi Srivastava [a,c], Shivesh Sabbarwal [a,b], Vivek Kumar Verma [a,c], Manoj Kumar [a,b,*]

[a] Nano2Micro Material Design Lab, IIT (BHU) Varanasi, India
[b] Department of Chemical Engineering & Technology, IIT (BHU) Varanasi, 221005, India
[c] School of Biomedical Engineering, IIT (BHU) Varanasi, 221005, India

HIGHLIGHTS

- Precisely computed high-temperature kinetic barrier (Jo) of nucleation using Vyazovkin AIC method.
- Thermogravimetric data was extracted from magnesium nanoclusters (~1 nm).
- Nucleation rate, frequency factor, ΔG, ΔH, and ΔS and interfacial surface energy of indigenously prepared magnesium nanoclusters was also estimated.
- Four different models were proposed for the computation of nucleation rate and interfacial energy of Magnesium nanoclusters.

ARTICLE INFO

ABSTRACT

The exploration of temperature-dependent nucleation is required to appraise the extent of kinetic and thermodynamic barriers associated with the origin of subatomic size nuclei, which controls the nucleation rate. The precise computation of nucleation rate, thermodynamic parameters, and interfacial surface energy for ultra-small nanoclusters (0.5–2 nm) is still absent in the high-temperature range. Here, apparent activation energy (E_a), thermodynamic parameters (ΔG, ΔH, and ΔS), and pre-exponential kinetic factor were estimated by utmost accurate Vyazovkin advanced, and KAS isoconversional techniques for calculation of nucleation rate and interfacial energy for ultra-small magnesium nanoclusters (~0.8 ± 0.24 nm), in the temperature range from 555 to 780 K. The master plots propounded the existence of third order random nucleation in magnesium metal matrix over a specified conversion. Based on the above findings, four mathematical models are proposed to compute nucleation rate and interfacial energy in magnesium clusters over respective temperatures and conversions. These models are beneficial for predicting the nucleation rate and interfacial energy over a high range of temperature and specific conversion.

1. Introduction

Nucleation is an elementary and crucial step toward forming sub-molecular-sized nuclei by the evolvement of high-temperature solid-state reactions or supersaturation (Joop and Sefcik, 2020). These nucleations occur through the process of crystallization, growth, phase alteration, and heating, abbreviated as heterogeneous nucleation (Li and Jun 2018). The knowledge of kinetic and thermodynamic barriers is of utmost importance to exploring the nucleation pathways, which simplifies the whole nucleation scenario understandable and lucid. Subsequently, the current research is centered on understanding nucleation rates by examining kinetic and thermodynamic barriers during solid-state reactions at high temperature. Good hold on the calculation of kinetic and thermodynamic barriers is required to compute the nucleation rate at high temperatures. Nucleation rate is the product of kinetic barrier ($J_0 = A \exp(E_a/RT)$) and thermodynamic barrier ($\exp(\Delta G/RT)$), where E_a is the activation energy of nucleation, ΔG is the thermodynamic barrier, and T is the varying temperature (Li and Jun 2018). Especially during the computation of nucleation rate, the accurate value of kinetic barrier (J_0) is barely known, and many scientific communities accorded J_0 as a constant term. For example, J_0 is calculated at room temperature as D/5d, D,

* Corresponding author.
  E-mail address: manojk.che@iitbhu.ac.in (M. Kumar).

and d is the diffusion coefficient and diameter of monomers, respectively (Li and Jun 2018).

On the other hand, in other approaches, J_0 at room temperature is calculated by using atomic force microscope (Henrique et al., 2015). For example, the value of J_0 in the case of silica nucleation on the substrates of NH3/COO– and carboxyl mixed hybrid were $10^{14.8}$ and $10^{13.5}$ nuclei m^{-2} min^{-1}, respectively (Wallace et al., 2009). However, for other nucleation systems, such approaches for calculating J_0 are still missing and no accurate method is available for calculating J_0 at high temperatures. The kinetic computations for nucleation and growth rate were often ignored due to the complexity involved in reaction rate computation and microscopic estimations (Carpenter and Grünwald, 2021). Therefore, the kinetic barrier J_0 is evaluated precisely by apparent activation energy of nucleation (E_a) and pre-exponential kinetic factor (A) at high temperatures. These A and E_a are calculated precisely at high temperatures by accurate isoconversional method using non-isothermal TGA data. Till now, InSe, crystallization was monitored at higher temperatures (40 $^\circ$C–550 $^\circ$C) by using isoconversional methods via TGA technology (Oyelaran et al., 1996). The calcite nucleation was investigated at 315 $^\circ$C, and the corresponding activation energy of nucleation was computed. Metal nanocrystal nucleation and growth were examined by incrementing the temperature from 20 $^\circ$C to 100 $^\circ$C. Despite the observation of nucleation of metal crystals in a narrow temperature range (20 $^\circ$C to 100 $^\circ$C) and InSe crystallization-based nucleation in a high-temperature range, no computation of Kinetic barrier J_0, Pre- exponential kinetic factor (A), nucleation rate, thermodynamic parameters ($\varDelta G$, $\varDelta H$, and $\varDelta S$) and interfacial energy was attempted. . Thus, the computation of accurate activation energy (kinetic determination) of inorganic nanomaterials is required to estimate nucleation rate precisely at high temperatures.

Over the centuries, the kinetic determination of inorganic materials has been vastly investigated to render solid and gaseous product formation. In the current scenario, various models were proposed for the determination of apparent activation energy precisely. In the first step, inorganic material's mass loss concerning temperature is extracted through a TGA machine, and the kinetic barrier of nucleation, i.e., activation energy, is obtained through the utmost accurate Vyazovkin advance isoconversional approach. Various scientific communities proposed mathematical models, such as KAS, Tang, and Starink methods for calculating apparent activation energy. But these methods are based on approximations. Despite that, in the Vyazovkin approach, activation energy values were averaged from 0 to α. Thus, the Vyazovkin AIC technique removes approximations and does not have an average activation energy value. Consequently, as the integrated approach, Vyazovkin AIC technique contains no systematic error (Vyazovkin, 2001) over the range of $\varDelta\alpha$ as compared to the KAS, Tang, Starink, and Vyazovkin approaches. Therefore Vyazovkin AIC technique is used to compute the apparent activation energy of nucleation, i.e., kinetic barrier for inorganic materials over the specified conversion and corresponding thermodynamic parameters at high temperature.

Currently, several inorganic materials like alkaline earth metals have attracted substantial scientific attention owing to their exceptional high interfacial energy, accelerated chemical reactivity, commercial availability, and biocompatibility (Ray et al., 2021). Due to these properties, they have been popularly used in the area of biosensing, optoelectronics (Jebur et al., 2019), catalysis (Yin et al., 2015), energy storage (Yartys et al., 2019), and displays (Duan and Liu, 2019). Especially, calcium and magnesium-based nanomaterials have captivated much attention due to their anomalous properties such as low densities and high specific strength (Wang and Li, 2018), aging resistance, recyclability, suitable mechanical property and better thermal and electrical conductivity (Mordike and Ebert, 2001). Subsequently, new synthetic routes

yielding materials with new properties are widely reported. In most of these reports, the primary focus is pinned on obtaining highly uniform size nanomaterials with a high degree of reproducibility. For instance, reports on thermal stability, nucleation rate, and interfacial energy related to magnesium nanomaterials have not been investigated to date. Therefore, an attempt has been made to evaluate the nucleation rate and interfacial energy of metallic magnesium nanocluster at high temperature.

For this purpose, MgNCs were synthesized using a commercially available BSA and ascorbic acid. Recently, Bovine serum albumin has been extensively utilized for synthesizing nanomaterial due to its peculiar ability to control nucleation and growth of nanosystem (Lillo et al., 2020; Sabbarwal et al., 2020; Wang et al., 2014). Hence, we acquired BSA as a model protein due to the presence of a disulfide bond and free cysteine, which provide stearic protection to the nanoclusters.

Currently, many researchers have adopted several approaches to acquire thermodynamic and kinetic parameters to investigate the nucleation rate and interfacial energy of the alkali earth metal-based nanomaterial. In line with this, *in situ* determination of interfacial energies between heterogeneously nucleated calcite and quartz (Fernandez-Martinez et al., 2013), non-isothermal degradation kinetics estimation of nanosized calcite (Ray et al., 2021), homogeneous nucleation of magnesium hydroxide (Klein et al., 1967), twin nucleation and growth study in the single crystal magnesium under dynamic loading (Kannan et al., 2018) and estimation of nucleation and growth mechanism of nanosized magnesium hydride from the help of hydrogen sorption kinetics (Mooij and Dam, 2013) have paved a solid foundation for investigating the nucleation rate and interfacial energies of the magnesium nanoclusters, which was used as a precursor for high-temperature studies.

Further, to the best of our knowledge, the kinetic energy barrier J_0 for the nucleation of magnesium cluster (MgNCs) of size 1–2 nm at high temperature was computed by the highly accurate Vyazovkin AIC approach for the first time. The solid-state reaction mechanism of MgNCs at high temperature was investigated utilizing $Z(\alpha)$ master plots. Thus, by visualizing the kinetic reaction mechanism steps of MgNCs through $Z(\alpha)$ master plots, random nucleation within the MgNCs matrix was confirmed. Consequently, a new mathematical model was proposed at a high temperature and respective conversions to compute the nucleation rate and corresponding interfacial energy of MgNCs for the first time with the aid of TGA data. On the contrary, the existence of thermodynamic barriers (thermodynamic parameters) within the MgNCs matrix was also computed using the precise value of kinetic energy barrier, i.e., activation energy.

2. Theoretical background for determination of kinetic parameters:

2.1. Thermogravimetric analysis (TGA):

Thermogravimetric analysis on MgNCs powder was carried out between 300 K and 962 K at three different heating rates of 10, 15, and 20 °C/min to evaluate the thermal stability and kinetics parameters under a nitrogen atmosphere (20 ml/min). The transformational activation energy at each conversional point is mathematically computed using different model-free isoconversion methods. Next, the master plot $(Z(\alpha))$ was obtained by examining the solid-state transformation reaction mechanism by plotting $Z(\alpha)$ versus conversion (α). Where $Z(\alpha)$ is the product of differential function $[f(\alpha)]$ and integral function $[g(\alpha)]$. The reaction mechanism is identified by following the experimental curve plotted on

the master curve. Fig. 3 shows clearly that the experimental data follows third-order random nucleation.

2.2. Kinetic study

The rate of reaction of thermal degradation and conversion (α) with the time (t) of MgNCs can be described by Eqs. (1) and (2). (Henrique et al., 2015).

$$\frac{d\alpha}{dt} = K(T)f(\alpha) \tag{1}$$

$$\propto = \frac{W_{0-}W_t}{W_0 - W_f} \tag{2}$$

Were, $K(T) = A \exp\left(\frac{-E_\alpha}{RT}\right)$

$K(T)$ = Rate constant of reaction

Where K (T) is the temperature (T) depending constant and t is reaction time, $f(\alpha)$ is a function suggesting the change in reaction rate constant with the extent of conversion (α), W_o and W_f are the initial and final weight of the sample, whereas W_t is the weight of sample at a particular time (t).

Arrhenius equation describes the correlation between the rate constant of the reaction and temperature. Thus the decomposition rate of the solid can be described as follows in Eq. (3). (Zabihi and Khodabandeh, 2013).

$$\frac{d\propto}{dt} = Ae^{\frac{-E_a}{RT}}f(\propto) \tag{3}$$

The pre-exponential factor is denoted as A, e_a is the Arrhenius activation energy, and R is the universal gas constant (8.314 KJ/mole).

Further, the decomposition rate of the reaction described by Eq. (3) is transformed into a non-isothermal rate expression, Eq. (4), to relate the rate of reaction as a function of temperature at a constant heating rate (β).

$$\frac{d\propto}{dt} = \frac{A}{\beta}e^{\frac{E_a}{RT}}f(\alpha) \tag{4}$$

where β is the constant heating rate.

Eq. (4) integration by separating variables gives Eq. (5) as mentioned below.

$$\int_0^x \frac{d\alpha}{f(\alpha)} = g(\alpha) = \frac{A}{\beta}\int_{T_0}^T exp(\frac{-E_a}{RT})dT \tag{5}$$

If T_0 corresponds to the initial temperature where the decomposition rate cannot be evaluated, the lower boundary of the integral disappears.

By substituting the $X = \left(-\frac{E_a}{RT}\right)$ in Eq (5), then rearranged Eq (6) described as follows.

$$g(\alpha) = \left(\frac{AE_a}{\beta R}\right)\left\{-\frac{exp^x}{x} + \int_0^\infty \left(\frac{exp^x}{x}\right)dx\right\} = \left(\frac{AE_a}{\beta R}\right)^{p(x)} \tag{6}$$

where g (α) is the integral function of conversion (α) and p(x) is the temperature integral, Eq (6) does not have an exact analytical solution. Most isoconversional kinetic models have been derived using Eq (4).

From the year 1960 s, significant contributions were made for development of various mathematical models to determine the kinetics of the solid system. Two mathematical techniques were basically adopted for computation of kinetic triplet (activation energy (E), frequency factor (A) and order of reaction (n)). These two mathematical techniques were basically model fitting as and model free technique.

Model fitting mathematical technique was used basically to compute the Arrhenius kinetic triplet (E, n and A) by adopting already predicted models $f(\alpha)$ like geometrical contraction models nucleation models, nucleation and growth models, reaction order-based models and diffusion models. Coats Redfern method is widely used non-isothermal model fitting technique to predict activation energy variation with heating rate. The temperature integral in the eq. (5), is approximated as $g(\alpha)$ is adopted through predefined models. Such technique is successful in prediction of activation energy at respective heating rate.

Thus model-fitting methods can predict the reaction kinetics with respect to heating rate. However, for the non-isothermal decomposition process, these predictions of kinetics by model fitting approach is supposed to have less accurate due to variation of K (T) with T during non-isothermal operation. This reproduction of kinetic parameters that strongly depend on the $g(\alpha)$ models for non-isothermal run can create many doubts in the calculated values of activation energy, which raises doubts about the physical meaning of these values. The applicability of model fitting method for computation of kinetics basically relies on the isothermal experiments, where (T) is a constant with temperature. Here, both (T) and (α) in eq. (5) govern the reaction rate of isothermal experiment. However, during the isothermal run, (α) variation with α being less prominent than the (T) variation with T.

On the other hand, Model free techniques (i.e., isoconversional approach) relies on the calculation of kinetic parameters with respect to conversion and is basically free from any pre-defined reaction models. At different heating rate, T_α is chosen at particular point of conversion, and without use of any pre-defined integral based models i.e., $g(\alpha)$, the activation energy is calculated accurately for non-isothermal run.(Kumar et al., 2019).

Various isoconversional approaches were adopted for computation of kinetic parameters. Starink presented a detailed review of different techniques to get $E\alpha$, and basically-two groups were divided (Type 1) and p(I)-isoconversional methods, (Type 2), where I is ($-E_\alpha/RT$). The method in Type 1 is free of any approximation but Type 1 method is dependent on the variation reaction rate with individual stages of reaction at different heating rates. This Type 1 method is abbreviated as Friedman et al. (Dhyani et al., 2017). The main disadvantage of such method is fluctuation of activation energy with conversion. The other one is Type 2 method, which strongly depends on the approximation of the temperature integral in Eq. (5). These different isoconversional methods includes Kissinger (Dhyani et al., 2017), FWO (Kumar et al., 2021) and Starink techniques (Starink, 2003).

Apart from above mentioned types, there are other isoconversional methods that are free from any type of approximation and are more accurate. For instance, Vyazovkin proposed a model, that depend on function minimization for computation of activation energy with respect to conversion and abbreviated as model free method (Vyazovkin, 2001, 1997). But, as already explained, in Vyazovkin approach the activation energy got averaged with respect to conversion. Thus, we adopted Vyazovkin advanced isoconversional (V. AIC) method, which is free of any type of approximation and temperature integral is solved by trapezoidal rule. Due to integration of temperature integral by trapezoidal rule in small interval ($\Delta\alpha$), the accuracy in the computation of activation energy get enhances. In our investigation, $\Delta\alpha$ is taken to be 0.005. Thus, we used V.AIC isoconversional model free method in our study.

In this study, we used Flynn-wall-Ozawa (FWO), Kissinger (KAS), Starink, Tang, Vyazovkin, and Vyazovkin AIC methods to evaluate kinetic parameters at each conversion point, and $Z(\alpha)$ master plot were employed to gain insight the reaction mechanism followed by the thermal degradation process.

The Kissinger-Akahira-Sunose (KAS) (Kissinger, 1957) method is a differential isoconversional method, generally used to predict

the kinetic parameters such as Arrhenius activation energy (Ea.), frequency factor (A), and order of reaction (n) at each conversion. An Assumption $p(x) = X^{-2} e^{-X}$ was utilized to determine the following equation.

$$ln\frac{\beta}{T^2} = ln\frac{AE_\alpha}{Rg(\alpha)} - \frac{E_\alpha}{RT} \tag{7}$$

where β is the constant heating rate.

The slope of the plot between $ln\frac{\beta}{T^2}$ vs $\frac{1}{T}$ gives the activation energy at each conversion value (α).

The Flynn-Wall-Ozawa method (Flynn, 1997) is an integral isoconversional method that uses Doyle's empirical approximation instead of the temperature integral.

$$log\beta = log\frac{AE_\alpha}{Rg(\alpha)} - 2.315 - 0.4567\frac{E_\alpha}{RT} \tag{8}$$

The exponential value $p(x) = -2.315 + 0.457x$ were evaluated using Eq (8), and the slope of the linear plot between $log\beta$ vs $\frac{1}{T}$ yielded E_a/R.

By combining KAS and FWO methods, Starinks (Starink, 2003) proposed the following method:

$$ln\left(\frac{\beta}{T_\alpha^S}\right) = C - \frac{BE_\alpha}{RT_\alpha} \tag{9}$$

Using integral temperature approximation, Starink calculated the value of S and B as 1.92 and 1.0008, respectively, and put them in the above equation (9) to achieve reformed Eq. (10) (Gajera and Panwar, 2019)

$$ln\left(\frac{\beta}{T^{1.92}}\right) = const - 1.0008\left(\frac{E_\alpha}{RT}\right) \tag{10}$$

At each conversional point, the plot between $ln\left(\frac{\beta}{T^S}\right)$ and $\frac{1}{T_\alpha}$ gives a straight line, with a slope $\left(-1.0008\frac{E_a}{R}\right)$ that can be utilized to obtain activation energy.

In the Tang method (Wanjun et al., 2006) the apparent value of activation energy is calculated using the following Eq (Kumar et al., 2021).

$$ln\left(\frac{\beta}{T^{1.894661}}\right) = C_1 - 1.001450\frac{E_\alpha}{RT} \tag{11}$$

At the conversional point 0.1 to 0.9, a plot between $ln\left(\frac{\beta}{T^{1.894661}}\right)$ vs $\frac{1}{T_\alpha}$ gives a straight line with a slope $1.001450\frac{E_\alpha}{R}$.

Vyazovkin (Vyazovkin, 1997) is a non-linear isoconversional method, generally used to increase the accuracy of the activation energy of the system. This method depends on Eq. (12) for the evaluation of the activation energy (Ea) at a particular value of conversion (α), which minimizes the following function.

$$\varnothing = \sum_i^n \sum_{j\neq i}^n \frac{I(E_\times T_{\alpha,i})\beta_j}{I(E_\alpha, T_{\alpha,j})\beta_i} = min \tag{12}$$

$$I(E_\alpha, T_\alpha) = \int_0^{T_\alpha} exp\left(\frac{-E}{RT}\right)dT \tag{13}$$

The numerical value of activation energy at a particular conversion was obtained by substituting the experimental T and β into Eq. (13) and varying E_a to obtain the minimum value of the function. The accurate value of I (E_α, T_α) were evaluated with the help of the Senum-Yang approximation (Mishra and Bhaskar, 2014) (Senum and Yang, 1977). The same minimization procedure was repeated for each conversion (0.1–0.9), and the accurate activation energy at each extent of conversion was evaluated.

$$I(E_\alpha T_\alpha) = \frac{exp(-x)}{x} \cdot \frac{x^3 + 18x^2 + 86x + 96}{x^4 + 20x^3 + 120x^2 + 240x + 120} \tag{14}$$

Vyazovkin AIC (Vyazovkin, 2001)(advanced isoconversional) model is a modified version of the Vyazovkin model, which avoids the unwanted flattening of the Eα vs Conversion (α) curve.

In this modified integral isoconversional model, Ea is assumed for a small change in conversion (Δα), and the temperature integral is evaluated by varying Tα-Δα and Tα using the trapezoidal rule.

$$J(E_a, T(t)) = \int_{T_{\alpha-\Delta\alpha}}^{T_\alpha} exp\left(\frac{-E_a}{RT(t)}\right)dt \tag{15}$$

$$\varphi(E_a) = \sum_i^n \sum_{j\neq1}^n \frac{I(E_a, T_i(t_\alpha))}{I(E_a, T_j(t_\alpha))} = minimum \tag{16}$$

In Eq. (16), T_i (t) (i = 1...... n) is the actual variation of temperature, and the Ea into Eq. (16) varies until the minimum value of the function is reached.

2.3. Calculation of pre-exponential kinetic factor:

Isoconversional methods accurately computed the apparent value of activation energy, but these models are incompetent to predict the value of the solid-state reaction system's pre-exponential factor and reaction model. To obtain both the apparent activation energy and pre-exponential factor, the following modified Kissinger's Eq. (17) was used (Dhyani et al., 2017).

$$ln\left(\frac{\beta}{T_m^2}\right) = -\frac{E}{RT_m} + ln\left(\frac{AR}{E}\right) \tag{17}$$

where T_m represents the peak temperature of the DTG curve at all the heating rates.

As we know, the KAS method is based on different heating rates and gives a single apparent value of activation energy for the overall reaction conversion. Therefore, this method is not suitable for computing activation energy. Therefore, activation energy computed by the Vyazovkin AIC method is substituted in Eq. (18) to obtain a pre-exponential factor.

$$A_\alpha = \frac{\beta E_\alpha exp\left(\frac{E_\alpha}{RT_m}\right)}{RT_m^2} \tag{18}$$

A_α and E_α represent the value of the pre-exponential factor and apparent activation energy, respectively, at all the conversions point (0.1 to 0.9).

Computation of Thermodynamic Barriers of MgNCs for Initiation of Random Nucleation:

The computation of thermodynamic parameters allows us to interpret the system's feasibility (Singh et al., 2020). The apparent activation energy of MgNCs was obtained using six model-free isoconversional methods; among them, activation energy calculated from most accurate Vyazovkin AIC method is utilized to obtain frequency factor at different conversions by KAS method derived equation.

So, the following equation has been utilized for calculating pre-exponential factor and thermodynamic parameters such as ΔH, ΔG, and ΔS (Singh et al., 2021).

$$A = \beta E_\alpha exp\left(\frac{E_\alpha}{RT_m}\right) \tag{19}$$

$$\Delta H = E_\alpha - RT_\alpha \tag{20}$$

4

$$\Delta G = E_\alpha + RT_m In\left(\frac{K_b T_m}{hA}\right) \tag{21}$$

$$\Delta S = \left(\frac{\Delta H - \Delta G}{T_m}\right) \tag{22}$$

where K_b refers to the Boltzmann constant (1.381×10^{-23} JK^{-1}), h is Plank's constant (6.626×10^{-34} JS). T_m refers to peak temperature in the DTG curve. ΔH suggested the difference of energy between reactants and MgNCs activated complex. The change in entropy of the system (ΔS) measures the system's randomness, while average change in Gibbs energy (ΔG) represents the available free energy to the system.

Computation of Nucleation Rate, Kinetic barrier, Thermodynamic barrier, and Interfacial energy:

The nucleation rate of the upcoming solid phase (MgNCs) can be computed by Eq (23):

$$J = AJ_0 exp\left(\frac{-\Delta G^*}{RT}\right) = Aexp\left(\frac{-E_\alpha}{RT}\right)exp\left(\frac{-\Delta G^*}{RT}\right) \tag{23}$$

where J (μm^{-2} min^{-1}) represents nucleation rate in nuclei, R (J mol^{-1}K^{-1}) and T (J mol^{-1}) represent universal gas constant and temperature in K, respectively. ΔG represents the thermodynamic energy barrier, which is directly correlated to interfacial energy. The J_o in Eq. (23) represents the system's kinetic energy and can be expressed as $exp\left(\frac{-E_\alpha}{RT}\right)$.

Furthermore, the Thermodynamic parameter (Q) is stipulated by $\Delta G^*/RT$ and can be ascribed by the following equation (Li and Jun 2018).

$$Q = \frac{16\pi v_0^2 Y^3}{3(K_B T)^3} \tag{24}$$

where υ_0 represents the molecular volume of the nanomaterial given by $\frac{M}{\rho_{nm}N_A}$, where M and ρ_{nm} represent the nanomaterial's molar mass and density, and N_A is the Avogadro number. This particular Eq. (24) was utilized to obtain interfacial energy as a function of temperature and conversion.

Computation of atoms present in one cluster by using TEM data:

TEM images suggested the formation of spherical MgNCs.

Hence, $V_{cluster} = V_{atom} \times N_{atom}$

Were, $N_{atom} = (rc /ra)^3$

rc ($0.82/2 = 0.41$ nm) is the radius of MgNCs and ra is the radius of Mg atom (141 pm).

$V_{cluster}$ is the cluster volume, and V atom and N atom are the volume of atom and number of atoms in one cluster, respectively (Sabbarwal et al., 2020).

$$\left(\frac{4}{3}\right) \times \pi \times rc^3 = \left(\frac{4}{3}\right) \times \pi \times ra^3 \times N_A$$

3. Experimental sections

3.1. Chemical used:

Pure high-grade magnesium chloride salt (99.9 %) and L- ascorbic acid were purchased from Sigma Aldrich, and High-quality bovine albumin serum (98 %) was purchased from SRL. All mentioned chemicals were purchased from local suppliers and used as received without any adulteration.

3.2. Synthesis of MgNCs

All the glassware was washed with aqua regia and rinsed thoroughly with deionized water. In an optimal synthesis, bovine serum albumin (450 mg/ml, 1 ml) and magnesium salt solution (10 mM, 10 ml) were mixed in a 150 ml conical flask, followed by the addition of L-ascorbic acid (35 mg/ml, 3 ml) and kept for 2 hr at 55 °C under continuous stirring. The resultant light-yellow colored solution was further incubated for 15 hr at the same temperature to obtain newly synthesized metallic magnesium nanocluster (MgNCs). During the entire reaction process, the reacting system was tightly sealed to prevent oxidation of newly synthesized clusters.

3.3. Characterization

Prepared metallic magnesium nanocluster (MgNCs) was characterized using spectroscopic and microscopic techniques. The UV–vis absorbance spectra were recorded by using Elico SL210 spectrophotometer. The thermogravimetric analysis (TGA) at different heating rates (10, 15, and 20 °C/min) was carried out using a PerkinElmer STA 6000/TGA 4000(sample pans). Size of the prepared clusters was estimated with the help of High-resolution transmission electron microscopy (HR-TEM) of model FEI Tecnai G2 20 Twin with an accelerating electron beam voltage of 200 kV utilized, phase and crystallinity of the MgNCs were interrogated by using Brucker, Mode-D8 advance Eco XRD machine, XPS spectra were obtained with the assistance of FEI, Nova Nano SEM 450. Fourier transform infrared spectroscopy was carried out using Nicolet is5 (Thermo electron scientific instrument using KBr pellets in 4 K to 400 cm^{-1}) range, CD spectra were acquired by using CD Polarimeter J-500 circular dichroism spectrophotometer.

## 4. Results and discussion

Vacuum oven dried MgNCs (60 °C for 24 h) powder was used for XPS, FTIR, XRD, and TGA characterization, while size analysis was performed using an aqueous solution drop cast over a TEM grid.

4.1. UV–vis absorbance

Fig. 1 shows the UV–vis absorption spectra of BSA and BSA templated magnesium nanocluster. The absorption spectra of BSA displayed a sharp prominent peak at 280 nm designated to aromatic residue (Tryptophan, Tyrosine, and Phenylaniline) and disulfide bond (Patel and Mohanty, 2014; Topală et al., 2014), whereas the absorption spectra of BSA templated nanoclusters displayed a strong absorption in the UV region, which exponentially decay toward the visible region without the presence of any SPR band, this spectral phenomenon hint the formation of nanocluster with size range less than 2 nm (Lillo et al., 2020). No localized surface plasmon resonance peak in the 400–600 nm range of UV–vis spectra indicated the absence of larger-sized MgNCs (Li et al., 2019).

4.2. Size and phase analysis

The size distribution of developed BSA templated MgNCs was characterized by HRTEM, and the microscopic image was shown in Fig. 1, b. microscopic data analysis revealed that the average diameter of as-prepared clusters was 0.82 ± 0.24 nm, based on sampling more than 250 clusters. Additionally, the number of Mg atoms in a cluster is determined by utilizing TEM data and found 25 atoms in a cluster. Furthermore, phase purity and crystallinity of MgNCs were investigated by XRD analysis (Fig. 1, c). The XRD pattern of BSA templated MgNCs shows absence of any characteristic peak of magnesium, but displayed only one broad halo peak, which clearly indicated the amorphous nature of MgNCs due to ultrasmall size (<1nm).(Ghosh et al., 2014; Sabbarwal et al., 2020).

(a)

(b)

(c)

(d)
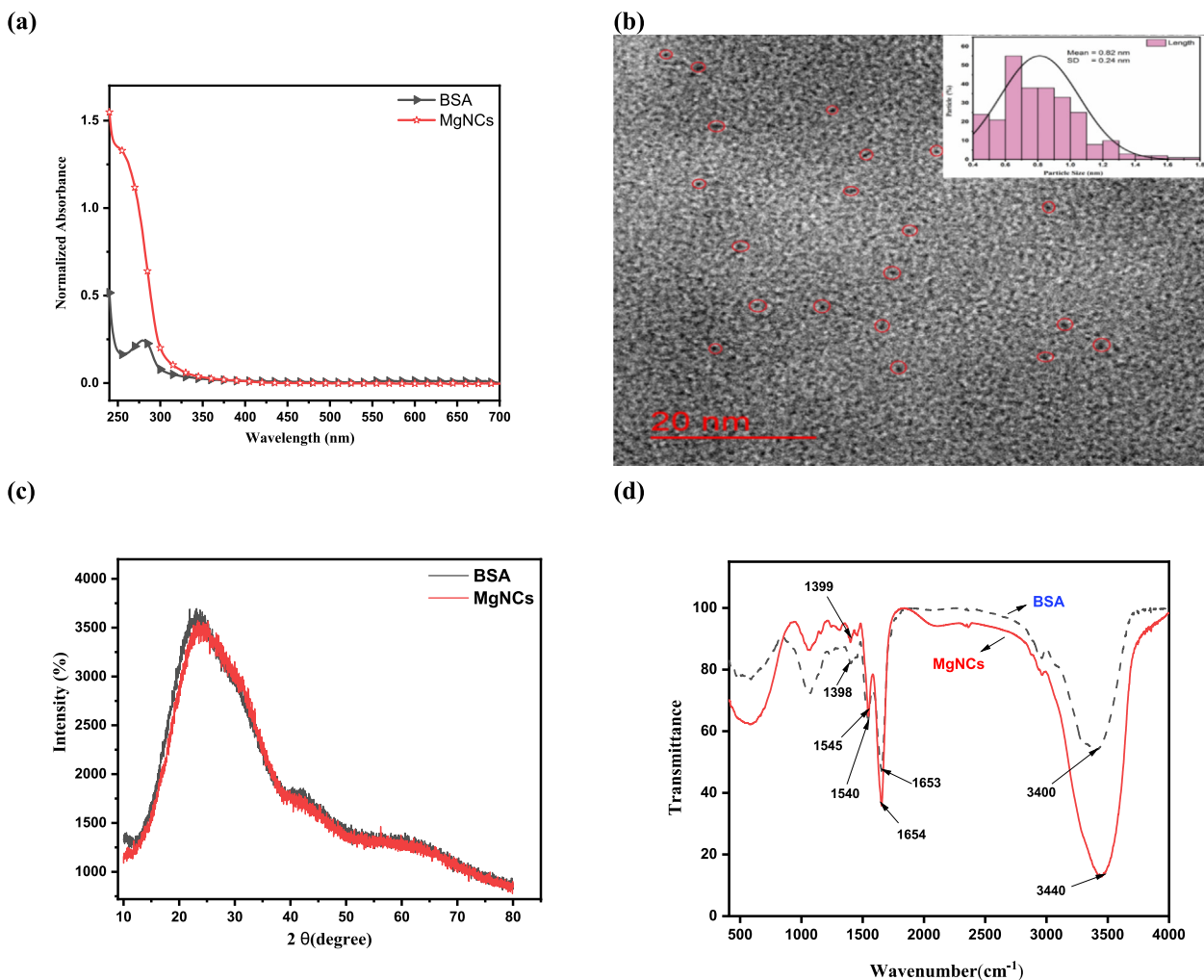
Fig. 1. (a) UV–vis absorption spectra of BSA and MgNCs, (b) HR-TEM image of the MgNCs at 50 nm scale bar inset Histogram with the distribution of MgNCs, (c) XRD of BSA and BSA capped MgNCs, (d) FTIR spectra of BSA and MgNCs.

4.3. Surface and infrared spectroscopy

The chemical composition and oxidation state of MgNCs were further investigated by XPS analysis; the high-resolution XPS spectra are shown in Fig. 2. The obtained spectra of C 1 s at 284.4 eV are used as reference spectra to adjust further and deconvolute the peak of interest. The C 1 s spectra of MgNCs deconvoluted into five peaks with binding energies at 284.4 eV (sp^2 hybridized carbon) (Mérel et al., 1998), 284.8 eV (sp^3 hybridized carbon)(Wu et al., 2007), 285.7 eV (C—N)(Zhang et al., 2013), 287.5 eV(C═O) (Nguyen et al., 1995) and 287.7 eV (C═O)(Ghodbane et al., 2010). XPS spectra of MgNCs were obtained and displayed in Fig. 2(a,b). The deconvoluted peak of Mg 2 s and Mg 1 s displayed a sharp prominent peak at 88.5 eV (Au and Roberts, 1985; Fuggle, 1977; Haider et al., 1975; Khalajabadi et al., 2017) and 1303.5 eV respectively (Fischer et al., 1991; Tajima et al., 2014; Yoshimura et al., 2004), attributed to metallic magnesium. The obtained XPS analysis result confirmed the successful grafting of MgNCs onto the BSA surface. FTIR spectra of BSA and BSA templated MgNCs are displayed in Fig. 1, d. The characteristic band of protein amide I (1600–1700), amide II (1480–1575), and amide III (1229–1301) is corresponded to C═O stretching, N—H bending and the combination of C—N and C—C stretching, and C═O bending (). The significant decrease in spectral intensities of amide I and II bands of BSA templated MgNCs compared to free BSA revealed the interac-

tion of Mg^{+2} with C═O, COO, and N—H functional groups of the protein. The binding interaction between BSA functional moieties (CN and N—H) and Mg^{+2} was further revealed by shifting the amide A band concerning free BSA (1653 cm^{-1} → 1654 cm^{-1}). However, the decrease in the spectral intensity of the amide I band concerning free BSA revealed the reduction of an alpha helix in the secondary structure of the protein (Alhazmi, 2019). A significant shift in spectra of MgNCs (3400 cm-1 → 3440 cm^{-1}) corresponds to the amide C═O band, resulting in the successful scaffolding of BSA onto MgNCs surface. The changes in conformation of BSA by reduction of an alpha helix was further confirmed by Circular dichroism study (Fig. 2d). (Zheng et al., 2014) The CD spectra of pure BSA and BSA templated MgNCs were carried out at 25 °C in the wavelength range between 190 nm and 290 nm. The spectra of BSA contain two bands at 208 nm and 222 nm, these bands are characteristic of π-π* and n-π* transition in the α helix of BSA. The α helix content of BSA and MgNCs was found to be 55.7 % and 22 % respectively. which demonstrate drastic change in the BSA secondary structure after MgNCs formation.(Patel and Mohanty, 2014).

4.4. Prediction of reaction kinetics and corresponding pathways

This work utilized a *Z*-master plot based on the p(u) method to identify the mechanism behind the thermal degradation pattern

(a)
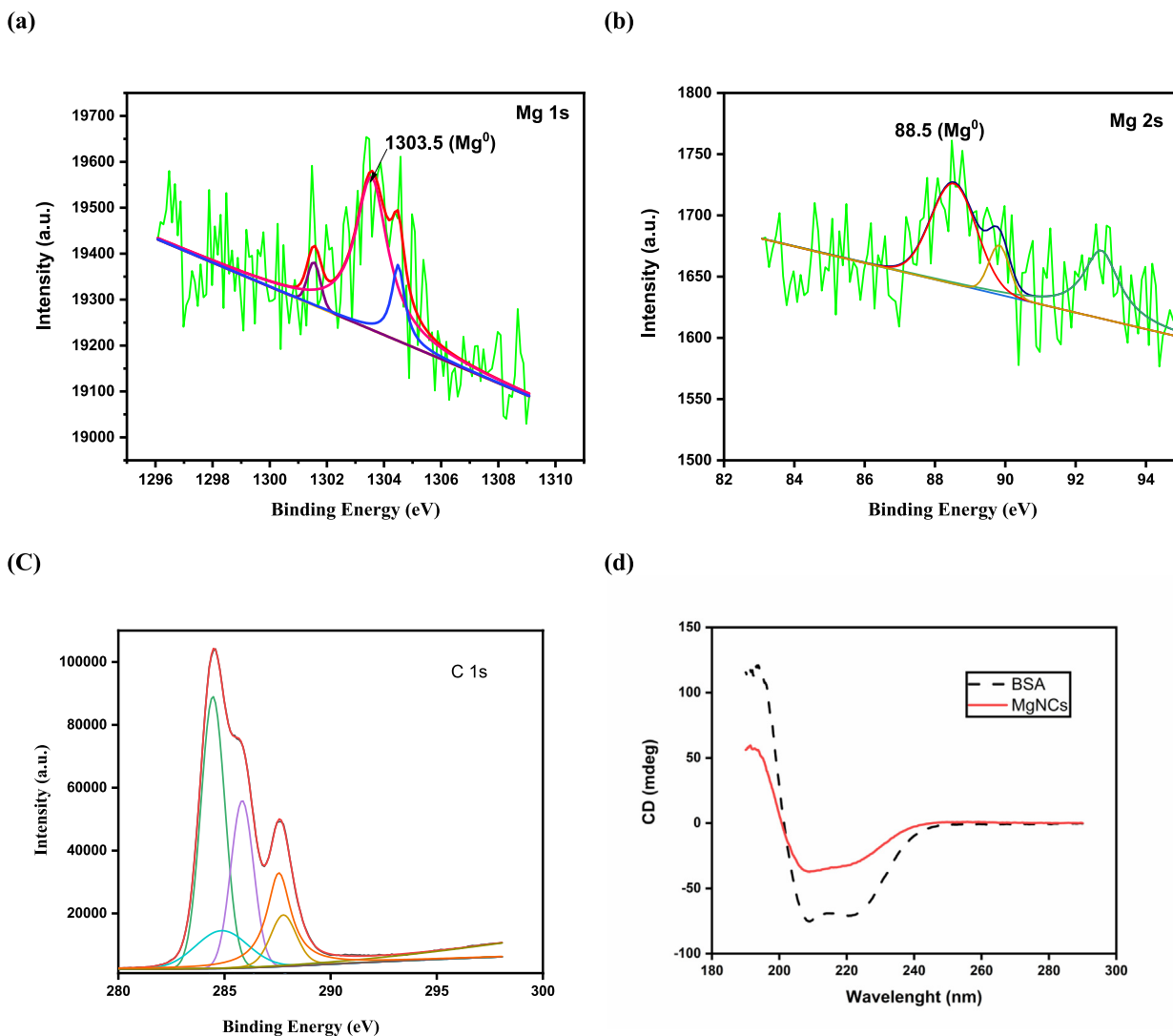
(b)

(C)

(d)

Fig. 2. XPS spectra of MgNCs (a) Mg 1 s (b) Mg 2 s (c) C1s (d) CD spectra of BSA and MgNCs.

and existing kinetics models based on integral and differential methods, as mentioned (ESI Table 5). The *Z*-master plot provided insight into the thermal degradation's mechanistic behavior as a function of conversion (α).

Calculated experimental data at each conversional point were compared with the theoretical model-derived data to obtain the reaction kinetics. The TGA data for the 10, 15, and 20 °C/min heating rates were fitted and plotted in a kinetic $Z(\alpha)$ master plot, which is a product of integral and differential function. The master plot is achieved by plotting $\frac{f(\alpha) \times g(\alpha)}{f(0.5) \times g(0.5)}$ as a function of conversions, i.e., by taking $\alpha = 0.5$ as a referral point.

The master plots for different solid-state reaction models are abbreviated by Khawam (Khawam and Flanagan, 2006).

For $\alpha = 0.5$, Eq. (25) can be written as:

$$z(\alpha) = \frac{f(\alpha) \times g(\alpha)}{f(0.5) \times g(0.5)} = \left(\frac{T_\alpha}{T_{0.5}}\right)^2 \times \frac{(d\alpha/dt)\alpha}{(d\alpha/dt)0.5} \qquad (25)$$

Afterward, plotted $Z(\alpha)$ master plot $\frac{f(\alpha) \times g(\alpha)}{f(0.5) \times g(0.5)}$ as a function of conversion (α) for the different dynamic oxidation models such as geometrical contraction model, nucleation models, diffusion models, and reaction order models and compared that with the experimentally obtained TGA data (Singh et al., 2020). It can be

clearly observed from Fig. 3 that in the conversional range from 0.1 to 0.9, the experimental $Z(\alpha)$ curve is closely following the theoretical curve of the *R*3 mechanism, which is linked to the 3 rd order random nucleation process (see Fig. 4).

4.5. Calculation of apparent activation energy concerning reaction conversion

Activation energy at each conversion point (0.1 to 0.9) was calculated by model-free isoconversional methods such as KAS, FWO, Starink, Tang, Vyazovkin, and Vyazovkin AIC method (Table 1). Fig. 5 a shows sinusoidal fluctuation in the activation energy of MgNCs as a conversion function. According to ICTAC rules, apparent activation energy variation should be around ± 5 % of the average activation energy value (Vyazovkin et al., 2011). Apparently, our computed activation energy is within this range (0.1–0.9) and very well complies with the recommendations. By visualizing the change in apparent activation energy as a function of conversion, five distinct phases were found to dominate during reaction conversion. In the first phase, for conversion ranging from 0.1 to 0.2, the apparent activation energy decreased from 164.6 to 153.41 kJ/mol. On the contrary, in the second phase, conversion between 0.2 and 0.3 activation energy increased from 153.41 to
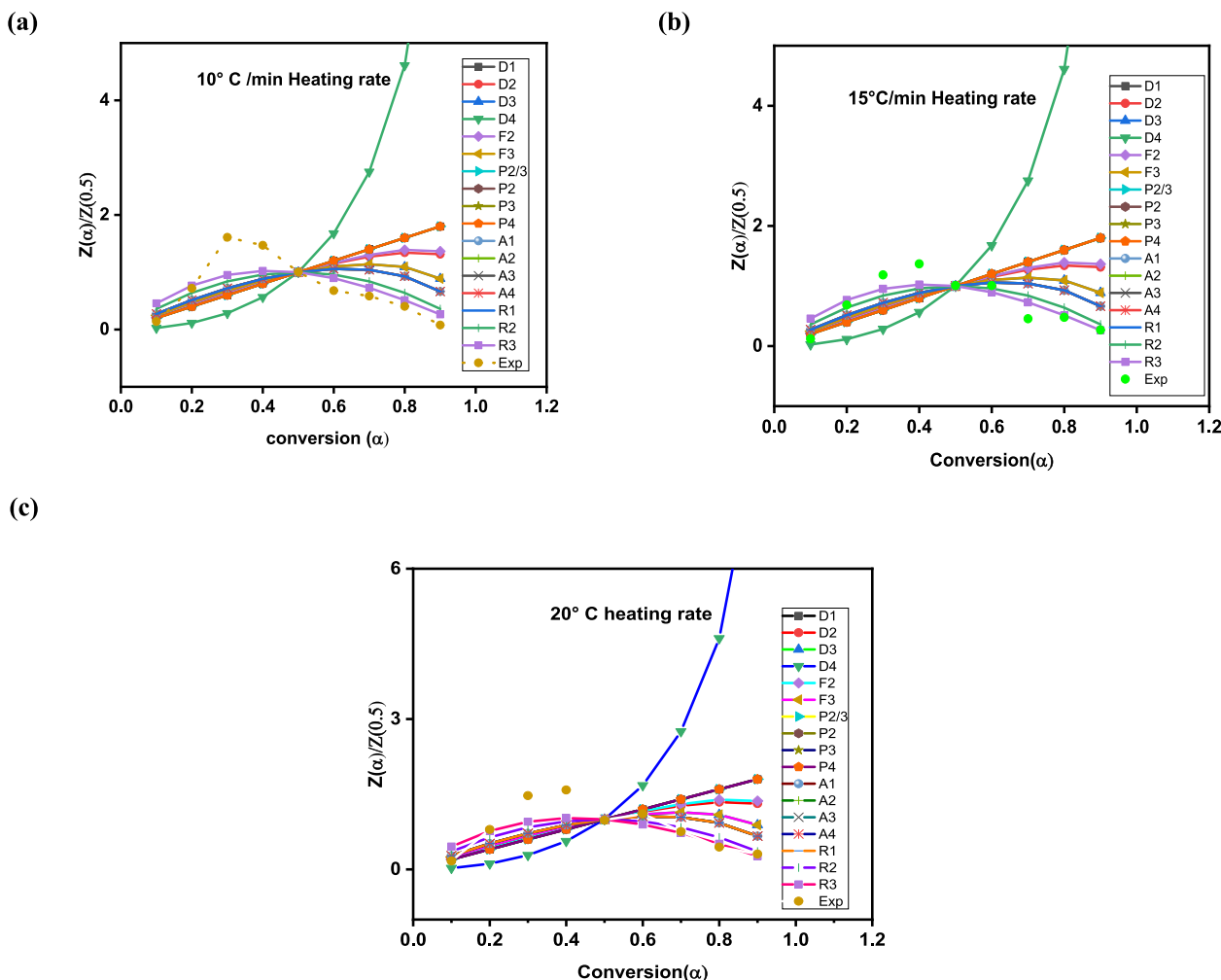
(a)

(b)

(c)

Fig. 3. (a) $Z(\alpha)$ master plot for estimation of thermal decomposition reaction mechanism of MgNCs at 10 °C/min (b) $z(\alpha)$ master plot for estimation of the thermal decomposition reaction mechanism of MgNCs at 15 °C/min (c) $z(\alpha)$ master plot for estimation of the thermal decomposition reaction mechanism of MgNCs at 20 °C/min.

201.7 kJ/mol. In the consecutive third to fifth reaction phases [(0.3–0.7), (0.7–0.8) and (0.8–0.9)], the apparent activation energy ranged from 201.7 kJ/mol-117.6 kJ/mol,117.6 kJ/mol-180.2 kJ/mol and 180.2–105.7 kJ/mol, respectively. The sinusoidal trend of apparent activation energy during the reaction progression is mainly due to the development of stable nuclei during the random nucleation process, along with the evolution and absorption of heat in reactions. Additionally, computed apparent activation energy was plotted against reaction progression to ensure the trend of reaction progression and acquire the overlapped activation energies value at each conversion.

The DTG and TGA curve of MgNCs plots Temperature against mass loss for all three heating rates, as shown in Fig. 8. To avoid undesirable reactions and oxidation of particles, a nitrogen atmosphere was utilized to create inert atmospheres. The DTG peak temperature increased from 592.05 → 604.15 K with an increment in the heating rate of 10 °C/min → 20 °C/min. It is analyzed that, for different heating rates (10, 15, and 20 °C/min), the mass loss rate of MgNCs (71.51 % →75.9 %) increased with an increase in heating rates. This is probably due to the BSA protein's heterogeneous and intricate nature (Norberto et al., 2012). Interestingly, an increment in the mass loss and the heat transfer rate is observed at higher heating rates more, due to the termination of the overall resistance barrier inside the MgNCs matrix and enhancement in mass loss(Evans and Strezov, 2000; Merabia et al., 2009).

4.6. Prediction of pre-exponential kinetic factor as a function of conversions

Fig. 5, b represents the variation of a pre-exponential factor with the reaction progression. A wide range of variations in the value of the pre-exponential factor suggests the complex and heterogeneous nature of the BSA matrix. Earlier studies have shown that the lower value of the pre-exponential factor ($A_\alpha < 10^9 s^{-1}$) manifested the less reactive system, and the nucleation process occurs only at the surface of MgNCs. While higher pre-exponential factor ($A_\alpha \geq 10^9 s^{-1}$) determines a highly reactive system, and the nucleation process occurs both from the core and surface of the MgNCs (Nawaz et al., 2021; Yuan et al., 2017).

4.7. Calculation of thermodynamic parameter against the reaction progression

Table 2 represents the value of thermodynamic parameters-ΔH, ΔG, and ΔS of MgNCs at all three heating rates, obtained by employing computed Apparent activation energy value (Vyazovkin AIC method). The change in enthalpy (ΔH) signifies the total heat content associated with the reacting system. The average ΔH value of MgNCs at 10, 15, and 20 °C/min was found to be 154.5 kJ/mol, 154.4 kJ/mol, and 154.3 kJ/mol, respectively, which is almost independent of heating rates; however, the positive value of ΔH
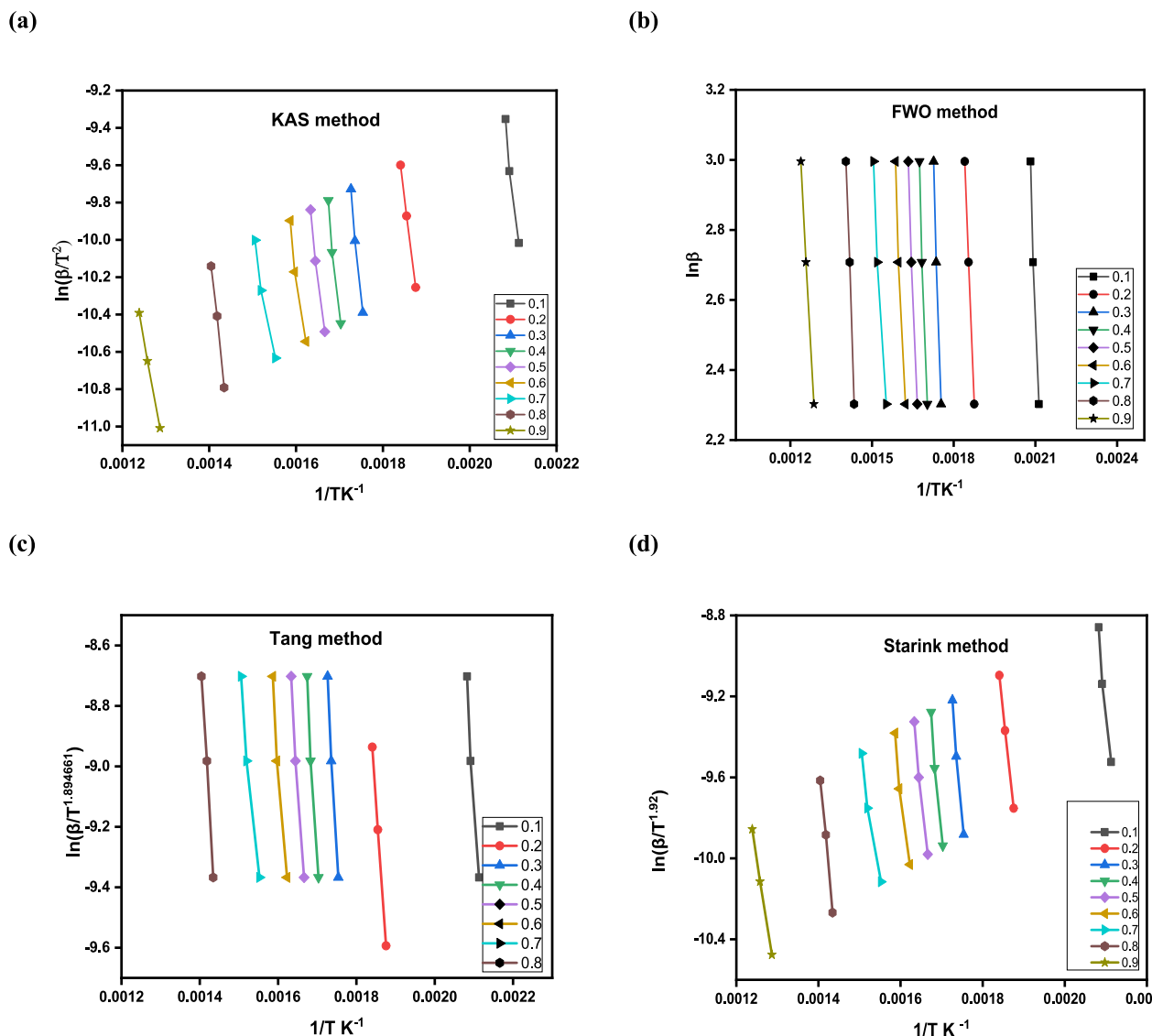
(a)

(b)

(c)

(d)

Fig. 4. Iso conversional models for kinetic analysis of MgNCs (a) KAS (b) FWO (c) Starink (d) Tang.

Table 1
Apparent value of activation energy (Ea) calculated using different iso-conversional models

Conversion (α)	Activation Energy (E$_\alpha$)					
	KAS	FWO	Starink	Tang	Vyazovkin	Vyazovkin AIC
0.1	172.9	180.9	173.29	173.3	173.15	164.62
0.2	155.26	164.2	155.62	155.7	155.4	153.41
0.3	197.2	206.85	197.68	198.34	197.5	201.7
0.4	184.77	194.62	185.16	186.5	185	189.7
0.5	162.26	172.33	162.66	165.2	162.54	171.40
0.6	143	153.40	143.4	147	143.38	151.8
0.7	107.9	118.79	108.3	113.8	108.37	117.6
0.8	180.13	191.84	180.6	184.12	180.47	180.2
0.9	106.8	119.99	107.36	115.10	107.4	105.7
Average	156.69	166.99	157.11	159.89	157.02	159.57

revealed endothermic nature of the reaction process. Although it is observed that ΔH strongly depends on reaction progression, especially for conversion 0.1 → 0.2, yielding an augmented value of ΔH. Whereas from 0.3 → 0.9 conversions, a sinusoidal pattern similar to activation energy was obtained (Fig. 6, b). The slight difference between ΔH and ΔE indicated the formation of the activated complex and also demonstrated the decrease in the endothermic nat-

ure of the reacting system as the reaction progressed. The change in Gibbs free energy with conversion at different heating rates is shown in Table 3. The change in Gibbs free energy (ΔG) indicated the reaction system's increased energy due to the formation of an activated complex (Singh et al., 2021). Although, ΔG at 10, 15, and 20 °C/min was found to be 154.4 kJ/mol, 153.9 kJ/mol, and 154.3 kJ/mol, which is positive, indicating unfavourable conditions
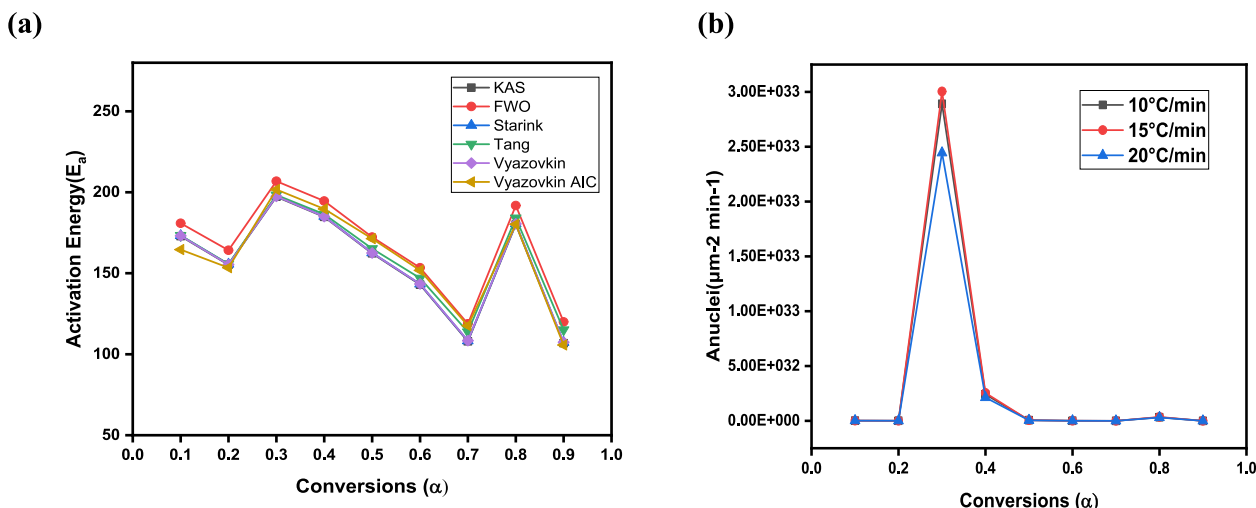
(a)

(b)

Fig. 5. (a) Comparison of apparent activation energies at all the conversions obtained from iso conversional models (b) Pre-exponential factor of MgNCs against conversions at all the three heating rates.

Table 2
Computed thermodynamic parameters required for MgNCs nucleation at different heating rates correponding to different coversion points

conversions (α)	Heating rate (10° C/min)				Heating rate (15° C/min)				Heating rate (20° C/min)			
	A (S⁻¹)	ΔH (KJ Mol⁻¹)	ΔG (KJ Mol⁻¹)	ΔS (KJ Mol⁻¹)	A (S⁻¹)	ΔH (KJ Mol⁻¹)	ΔG (KJ Mol⁻¹)	ΔS (KJ Mol⁻¹ K⁻¹)	A (S⁻¹)	ΔH (KJ Mol⁻¹)	ΔG (KJ Mol⁻¹)	ΔS (KJ Mol⁻¹ K⁻¹)
0.1	1.89×10^{14}	160.68	178.05	−0.02933	2.1×10^{14}	160.63	178.63	−0.03014	1.86×10^{14}	160.62	178.13	−0.029
0.2	1.81×10^{13}	148.98	151.54	−0.00432	2.04×10^{13}	148.92	150.96	−0.0034	1.86×10^{13}	148.89	151.46	−0.00424
0.3	4.35×10^{17}	196.98	150.19	0.079039	4.52×10^{17}	196.93	149.60	0.079272	3.67×10^{17}	196.91	150.08	0.077509
0.4	3.61×10^{16}	184.89	150.49	0.058102	3.83×10^{16}	184.83	149.90	0.058494	3.2×10^{16}	184.80	150.39	0.056967
0.5	7.8×10^{14}	166.41	150.99	0.02604	8.54×10^{14}	166.34	150.40	0.026685	7.46×10^{14}	166.31	150.90	0.025503
0.6	1.29×10^{13}	146.68	151.59	−0.00828	1.46×10^{13}	146.60	151.01	−0.00738	1.34×10^{13}	146.56	151.51	−0.00818
0.7	9.63×10^{9}	112.26	152.84	−0.06855	1.16×10^{10}	112.14	152.27	−0.06721	1.15×10^{10}	112.09	152.79	−0.06736
0.8	4.92×10^{15}	174.42	150.74	0.039995	5.31×10^{15}	174.36	150.16	0.040526	4.54×10^{15}	174.30	150.65	0.039147
0.9	7.79×10^{8}	99.30	153.37	−0.09133	9.55×10^{8}	99.15	152.80	−0.08985	9.72×10^{8}	99.05	153.32	−0.08984
Avg		154.51	154.42	0.000152		154.51	153.97	0.000777		154.39	154.36	5.54×10^{-5}

for the reaction. The increment in the average value of *ΔG* concerning heating rates indicated that the reacting process consumes more energy at a high heating rate, whereas the increase of *ΔH* (Fig. 6, a) with reaction progression suggested excess heat supplied to the reacting system (Dhyani et al., 2017).

The change in entropy (*ΔS*) measures a reacting system's randomness (Singh et al., 2020). Therefore, its variation as a function of conversion at different heating rates is presented in Table 2. The value of *ΔS* at 10, 15, and 20 °C/min is found to be 1.5 × 10⁻⁴, 7.7 × 10⁻⁴, and 5.5 × 10⁻⁵, respectively.

It was observed that *ΔS* for MgNCs has negative and positive values for the entire reaction course. The lower value of *ΔS* indicated the physical and chemical changes in MgNCs, bringing them to the state of thermodynamic equilibrium (Palmay et al., 2021). The graph of *ΔS* versus conversion is displayed in Fig. 6, c.

4.8. Dependency of nucleation rate in conversion and temperature:

In current scenarios, computation of nucleation rate was limited due to inadequate understanding of kinetic and thermodynamic parameters. Eq. (23) was employed to compute the rate of nucleation at high temperatures, but the kinetic term (*J₀*) in the equation was considered constant by several scientists (Fernandez-Martinez et al., 2013; Hamm et al., 2014). However, at high-temperature nucleation rate analysis, the value of *J₀* dominated. Hence predic-

tion of *J₀* is necessary to obtain an accurate value of nucleation rate (Thomas, 2007).

In this study, the kinetic term (*Jo*) has been computed by utilizing *A* and E_a, rather than assuming it as a constant value, to predict more accurate nucleation rate values at high temperatures.

Moreover, the value of apparent activation energy and pre-exponential kinetic factor (*A*) is computed by utilizing Vyazovkin AIC, and KAS derived equation, respectively; furthermore, for a better understanding of the nucleation process, understanding nuclei geometry is crucial (Li and Jun 2018). After incorporating the value of nuclei geometry in Eq. (23). This is accomplished by converting activation energy and kinetic factor (*A*) units into Nuclei μm⁻²·min⁻¹. This results in a significant change of *A* and *J* (nucleation rate) values, as nucleus volume and surface area get incorporated into the equation. (ESI. Table 1).

By visualizing graph 7(b) between *J* (Nuclei μm⁻² min⁻¹) and T (K), an increasing trend in nucleation rate as a function of temperature was observed. Additionally, nucleation rate was also computed concerning different heating rates (10, 15, and 20 °C/min) and observed an increasing trend with a rise in heating rate, and this phenomenon is due to a decrease in heat and mass resistance with an increase in temperature. (ESI table 2).

To acquire a relationship of nucleation rate with specific temperature and conversion, a theoretical model was deduced by fitting the experimental data. An exponential model $J = Q_1 exp\left(\frac{T}{\rho_1}\right) + Yo$ and $J = Q_2 exp\left(\frac{\alpha}{\rho_2}\right) + J_0$ were best fitted for the

(a)

(b)

(c)
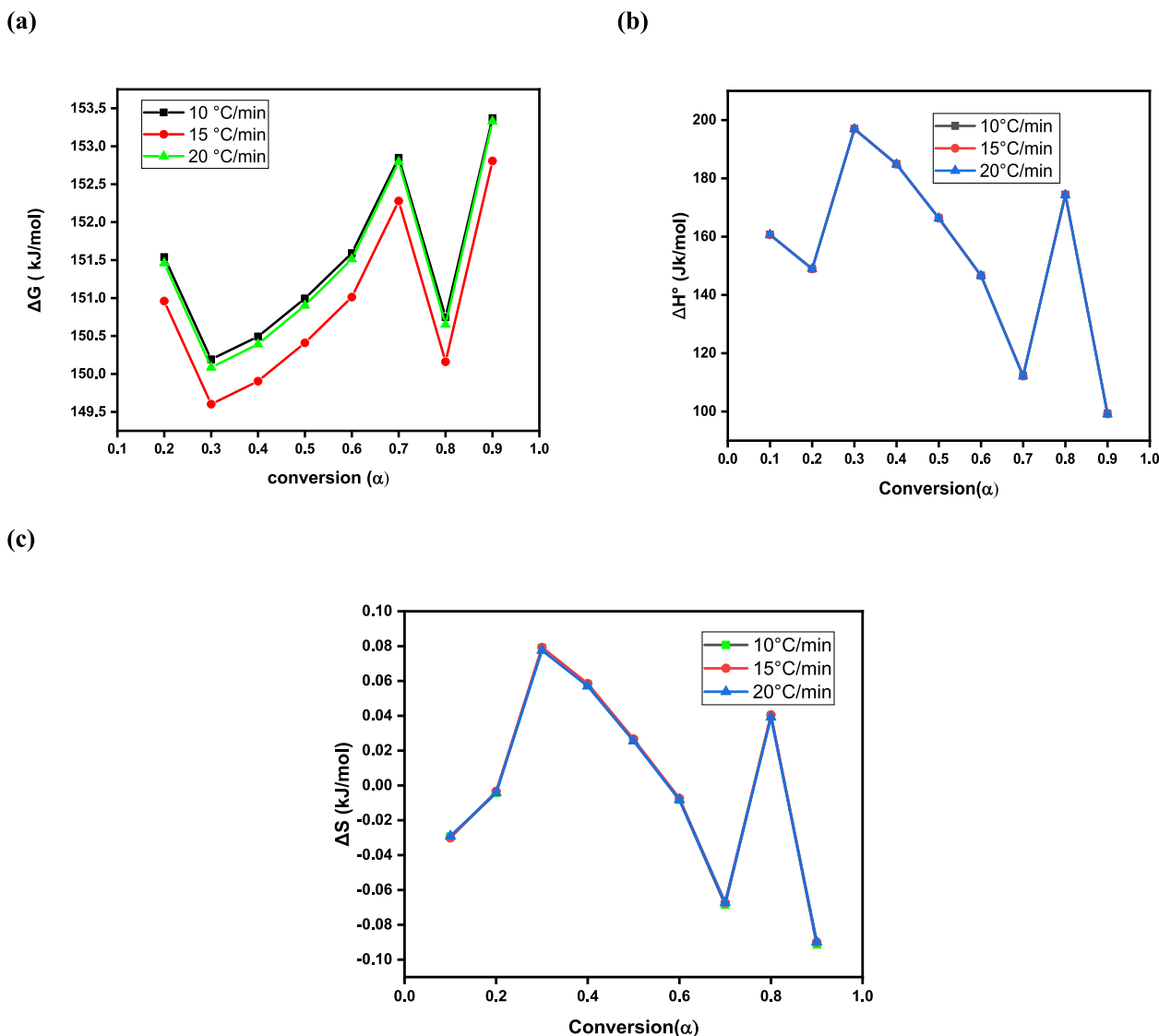
Fig. 6. (a) Plot between ΔG against Conversion at all three heating rates (b) Plot between ΔH against Conversion at all three heating rates (C) (c) Plot between ΔS against Conversion at all three heating rates.

temperature and conversion, respectively, at all three heating rates. Where Q_1, Q_2, ρ_1, and ρ_2 are exponential function constants, their values are shown in ESI table 4. The graph is shown in Fig. 7 a, b.

4.9. Variation of interfacial energy with temperature and reaction progression

Determination of interfacial energy of MgNCs in the BSA matrix is a crucial parameter in determining several physical quantities of interest (Jha et al., 2019). Until now, numerous experimental techniques have been carried out to determine interfacial energy (Li et al., 2014), such as the computation of interfacial energy of copper nanoparticles by using the galvanic cell method for a short range of temperature (750–950 K) (Gozzi et al., 2010), calculation of interfacial energy of calcite at room temperature (30–50 mJ/m^2) (Fernandez-Martinez et al., 2013; Li et al., 2014).However, no studies has been carried to determine interfacial energy of nanomaterials at high temperature utilizing TGA data. Apart from novel technique, we are very first to interpret interfacial energy of magnesium nanocluster in BSA matrix. In the current case 16 π/3 refers constant geometrical factor, derived from the homogeneous nucle-

ation of spherical particles (Li and Jun 2018). In contrary, for the heterogeneous nucleation process, 16π/3 is considered as numerical constant instead and facilitate comparison between the interfacial energy in case of homogeneous and heterogeneous nucleation, in place of suggesting spherical nuclei (Li and Jun 2018). In our study, it was observed that effective interfacial energy of MgNCs is increase with the rise in temperature, such as 111.75 → 148.01 mJ/m^2,112.8 → 150.09 mJ/m^2, 113.03 → 151.78 mJ/m^2 and at 10, 15 and 20 °C/min, respectively. Average estimated value of interfacial energy are found to be 125.95 (10 °C/min), 127.07 (15 °C/min) and 127.86 (20 °C/min).This obtained value are in good harmony with previously reported interfacial energy of alkaline earth metal-based nanoparticles (Fernandez-Martinez et al., 2013). In order to obtain temperature dependent effective interfacial energy, a theoretical model is developed and fitted with experimental data. To understand the mechanistic relation between apparent interfacial energy and temperature a best fitted liner model Y = a_1T + b_1 is developed, where a_1 and b_1 are linear function constant and their values are (0.1366, 41.88), (0.1357, 42.25) and (0.1353, 42.62) at 10, 15 and 20 °C/min, respectively. From the above-mentioned model, we deduced that the apparent interfacial energy is independent on heating rates. However, for the graph
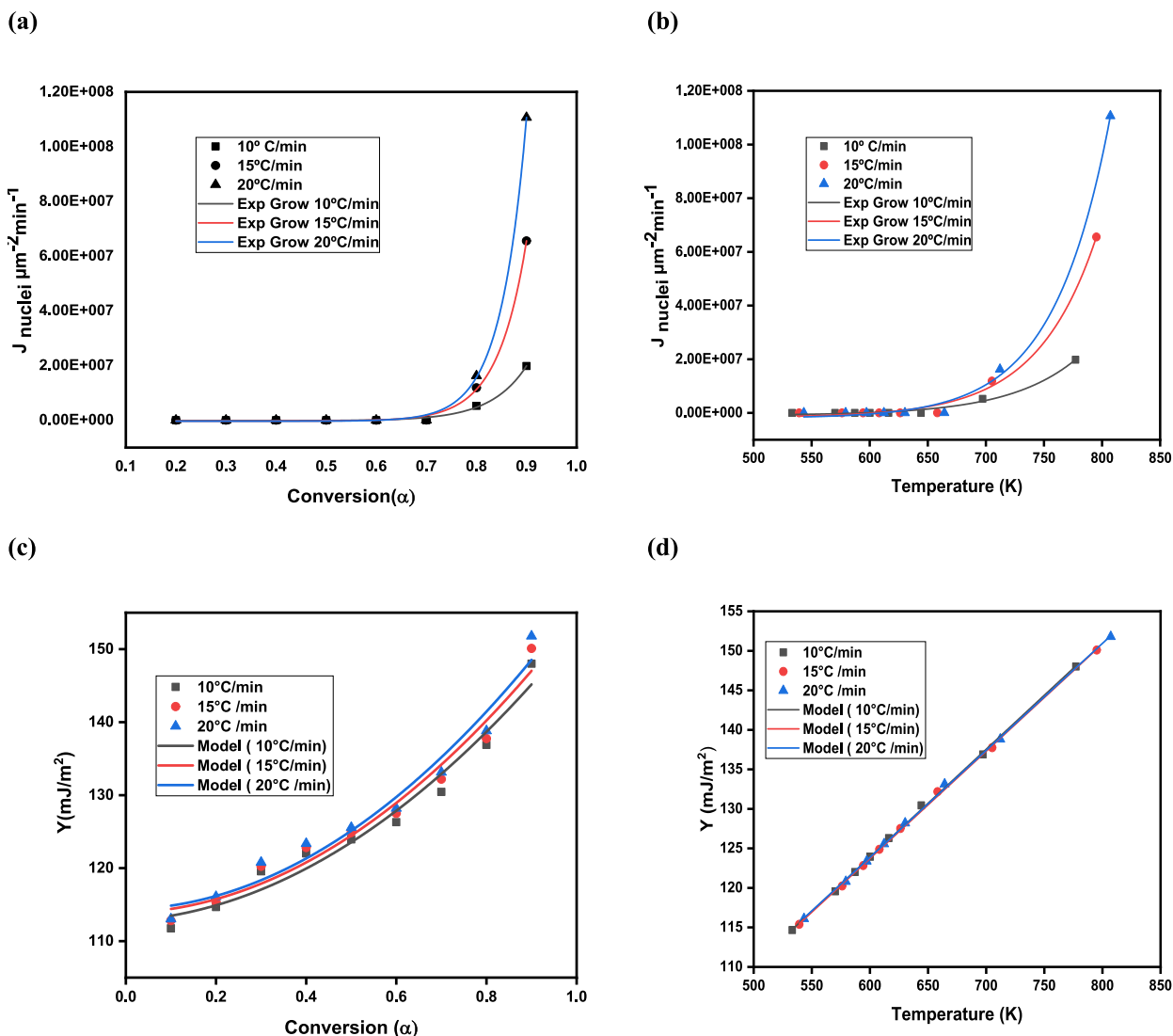
(a)

(b)

(c)

(d)

Fig. 7. (a) Plot between nucleation rate and conversion(α) (b) Plot between nucleation rate and Temperature(K) (c) Plot between interfacial energy and conversion(α) (d) Plot between interfacial energy and Temperature (K).

(Fig. 7, c) between interfacial energy versus conversion, suggests a second-order polynomial model ($Y = a_2T^2 - b_2T + R$) at all three heating rates. The values of a_2, b_2, and r at different heating rates 10, 15, and 20 ^{0}C/min, are found as (3.47 ± 13.80,36.15 ± 13.45,1 12.76 ± 3.0),(1.70 ± 13.9,39.0 ± 13.59,113.84 ± 3.03),and(1.00 ± 14.68,41.10 ± 14.31,114.3 ± 3.19),respectively. Analyzing this result, we find that as temperature increases, the nucleation rate also increases exponentially, due to increase in the effective value of interfacial energy. Graph displayed in Fig. 7, d.

5. Conclusion

The thermogravimetric analysis of metallic magnesium nanoclusters was carried out using TGA analyser at 10, 15 and 20 °C/min heating rates, under nitrogen atmosphere. Apparent activation energy (E_a), pre-exponential kinetic factor (A), nucleation rate (J), interfacial energy (Y) and thermodynamic parameters (ΔH, ΔG and ΔS) of ultrasmall MgNCs in BSA matrix were computed using most appropriate and accurate technique at high temperature. Furthermore, the differential function $f(\alpha)$ and integral form $g(\alpha)$ was found to vary as $(1-\alpha)^3$ and $[(1-\alpha)^{-2}-1]/2$ respectively, upon moni-

toring $Z(\alpha)$ master plot against experimental value. Moreover, the apparent value of activation energy calculated using the most accurate Vyazovkin AIC method was found to be 159.56 kJ/mol and further utilized to compute thermodynamic parameters. The lesser value of activation energy revealed the suitability in reaction progression, whereas the value of ΔH at different conversion points suggested the easier reaction progression via activated complex formation. The negative value of ΔS at some conversional points revealed that both chemical and physical changes in material are extended to reach thermodynamic equilibrium.

Further, the pre-exponential kinetic factor was also determined by utilizing KAS derived equation to obtain the nucleation rate at high temperature and specific conversions. For the first time, the Nucleation rate of MgNCs was investigated at found to be governed by $J = Q_1 exp\left(\frac{T}{\rho_1}\right) + Yo$ and $J = Q_2 exp\left(\frac{\alpha}{\rho_2}\right) + J_0$ models against high temperature and specific conversion, respectively. Additionally, interfacial energy for the MgNCs was also computed by utilizing a thermodynamic barrier and was governed by Y = a1T + b1 and Y = a2T2-b2T + R models at specific temperatures and conversions, respectively.

(a)

(b)

(c)
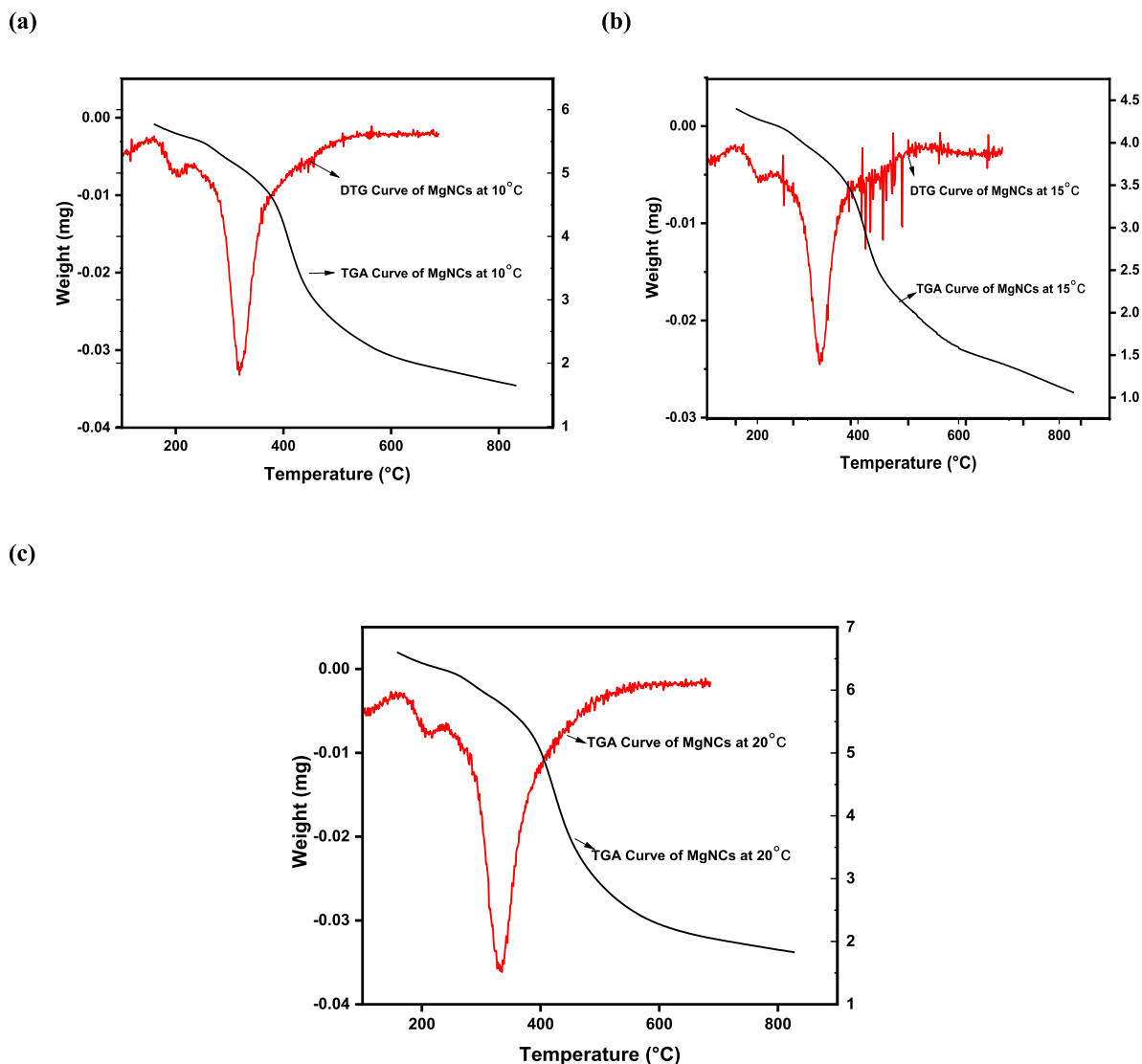
Fig. 8. (a) TGA and DTG curve of MgNCs at 10 °C/min heating rate (b) TGA and DTG curve of MgNCs at 15 °C/min heating rate (c) TGA and DTG curve of MgNCs at 20 °C/min heating rate.

Data availability

Data will be made available on request.

Declaration of Competing Interest

The authors declare that they have no known competing financial interests or personal relationships that could have appeared to influence the work reported in this paper.

Acknowledgment

Appendix A. Supplementary material

Supplementary data to this article can be found online at https://doi.org/10.1016/j.ces.2022.118223.

References

Alhazmi, H.A., 2019. FT-IR spectroscopy for the identification of binding sites and measurements of the binding interactions of important metal ions with bovine serum albumin. Sci. Pharm. 87. https://doi.org/10.3390/scipharm87010005.

Au, C.T., Roberts, M.W., 1985. Structure of the chloride overlayer at a magnesium surface. Surf. Sci. Lett. 149, 18–24. https://doi.org/10.1016/0167-2584(85)90786-8.

Carpenter, J.E., Grünwald, M., 2021. Pre-Nucleation Clusters Predict Crystal Structures in Models of Chiral Molecules. J. Am. Chem. Soc. 143, 21580–21593. https://doi.org/10.1021/jacs.1c09321.

Dhyani, V., Kumar, J., Bhaskar, T., 2017. Thermal decomposition kinetics of sorghum straw via thermogravimetric analysis. Bioresour. Technol. 245, 1122–1129. https://doi.org/10.1016/j.biortech.2017.08.189.

Duan, X., Liu, N., 2019. Magnesium for Dynamic Nanoplasmonics. Acc. Chem. Res. 52, 1979–1989. https://doi.org/10.1021/acs.accounts.9b00157.

Evans, T., Strezov, L., 2000. Interfacial heat transfer and nucleation of steel on metallic substrates. Metall. Mater. Trans. B Process Metall. Mater. Process. Sci. 31, 1081–1089. https://doi.org/10.1007/s11663-000-0083-2.

Fernandez-Martinez, A., Hu, Y., Lee, B., Jun, Y.S., Waychunas, G.A., 2013. In situ determination of interfacial energies between heterogeneously nucleated CaCO3 and quartz substrates: Thermodynamics of CO 2 mineral trapping. Environ. Sci. Technol. 47, 102–109. https://doi.org/10.1021/es3014826.

Fischer, A., Köstler, H., Schlapbach, L., 1991. Hydrogen in magnesium alloys and magnesium interfaces: preparation, electronic properties and interdiffusion. J. Less-Common Met. 172–174, 808–815. https://doi.org/10.1016/0022-5088(91)90207-K.

Flynn, J.H., 1997. The "temperature integral" - Its use and abuse. Thermochim. Acta 300, 83–92. https://doi.org/10.1016/S0040-6031(97)00046-4.

Fuggle, J.C., 1977. XPS, UPS AND XAES studies of oxygen adsorption on polycrystalline Mg at ∼100 and ∼300 K. Surf. Sci. 69, 581–608. https://doi.org/10.1016/0039-6028(77)90135-2.

Gajera, B., Panwar, N.L., 2019. Pyrolysis and kinetic behaviour of black gram straw using thermogravimetric analysis. Energy Sources, Part A Recover. Util. Environ. Eff., 1–14 https://doi.org/10.1080/15567036.2019.1662138.

Ghodbane, S., Ballutaud, D., Omnès, F., Agnès, C., 2010. Comparison of the XPS spectra from homoepitaxial 111}, {100 and polycrystalline boron-doped diamond films. Diam. Relat. Mater. 19, 630–636. https://doi.org/10.1016/j.diamond.2010.01.014.

Ghosh, R., Sahoo, A.K., Ghosh, S.S., Paul, A., Chattopadhyay, A., 2014. Blue-emitting copper nanoclusters synthesized in the presence of lysozyme as candidates for cell labeling. ACS Appl. Mater. Interfaces 6, 3822–3828. https://doi.org/10.1021/am500040t.

Gozzi, D., Tomellini, M., Lazzarini, L., Latini, A., 2010. High-temperature determination of surface free energy of copper nanoparticles. J. Phys. Chem. C 114, 12117–12124. https://doi.org/10.1021/jp1033867.

Haider, N.C., Alonso, J., Swartz, W.E., 1975. Valence and Core Electron Spectra of Mg in MgO in Evoporated Thin Films. Zeitschrift fur Naturforsch.ung – Sect. A J. Phys. Sci. 30, 1485–1490. https://doi.org/10.1515/zna-1975-1119.

Hamm, L.M., Giuffre, A.J., Han, N., Tao, J., Wang, D., De Yoreo, J.J., Dove, P.M., 2014. Reconciling disparate views of template-directed nucleation through measurement of calcite nucleation kinetics and binding energies. Proc. Natl. Acad. Sci. U. S. A. 111, 1304–1309. https://doi.org/10.1073/pnas.1312369111.

Henrique, M.A., Flauzino Neto, W.P., Silvério, H.A., Martins, D.F., Gurgel, L.V.A., Barud, H. da S., Morais, L.C. de, Pasquini, D., 2015. Kinetic study of the thermal decomposition of cellulose nanocrystals with different polymorphs, cellulose I and II, extracted from different sources and using different types of acids. Ind. Crops Prod. 76, 128–140. https://doi.org/10.1016/j.indcrop.2015.06.048.

Jebur, Q.M., Hashim, A., Habeeb, M.A., 2019. Structural, Electrical and Optical Properties for (Polyvinyl Alcohol-Polyethylene Oxide–Magnesium Oxide) Nanocomposites for Optoelectronics Applications. Trans. Electr. Electron. Mater. 20, 334–343. https://doi.org/10.1007/s42341-019-00121-x.

Jha, R., Diercks, D.R., Chakraborti, N., Stebner, A.P., Ciobanu, C.V., 2019. Interfacial energy of copper clusters in Fe-Si-B-Nb-Cu alloys. Scr. Mater. 162, 331–334. https://doi.org/10.1016/j.scriptamat.2018.11.039.

Joop, H., Sefcik, J., 2020. The Handbook of Continuous Crystallization, The Handbook of Continuous Crystallization. The Royal Society of Chemistry. https://doi.org/10.1039/9781788013581.

Kannan, V., Hazeli, K., Ramesh, K.T., 2018. The mechanics of dynamic twinning in single crystal magnesium. J. Mech. Phys. Solids 120, 154–178. https://doi.org/10.1016/j.jmps.2018.03.010.

Khalajabadi, S.Z., Abu, A.B.H., Ahmad, N., Kadir, M.R.A., Ismail, A.F., Nasiri, R., Haider, W., Redzuan, N.B.H., 2017. Biodegradable Mg/HA/TiO 2 nanocomposites coated with MgO and Si/MgO for orthopedic applications: A study on the corrosion, surface characterization, and biocompatability. Coatings 7. https://doi.org/10.3390/coatings7100154.

Khawam, A., Flanagan, D.R., 2006. Solid-state kinetic models: Basics and mathematical fundamentals. J. Phys. Chem. B 110, 17315–17328. https://doi.org/10.1021/jp062746a.

Kissinger, H.E., 1957. Reaction Kinetics in Differential Thermal Analysis. Anal. Chem. 29, 1702–1706. https://doi.org/10.1021/ac60131a045.

Klein, D.H., Smith, M.D., Driy, J.A., 1967. Homogeneous nucleation of magnesium hydroxide. Talanta 14, 937–940. https://doi.org/10.1016/0039-9140(67)80126-7.

Kumar, M., Srivastava, N., Upadhyay, S.N., Mishra, P.K., 2021. Thermal degradation of dry kitchen waste: kinetics and pyrolysis products. Biomass Convers. Biorefinery. https://doi.org/10.1007/s13399-021-01309-z.

Kumar, M., Sabbarwal, S., Mishra, P.K., Upadhyay, S.N., 2019. Thermal degradation kinetics of sugarcane leaves (Saccharum officinarum L) using thermogravimetric and differential scanning calorimetric studies. Bioresour. Technol. 279, 262–270. https://doi.org/10.1016/j.biortech.2019.01.137.

Li, Y., Feng, L., Yan, W., Hussain, I., Su, L., Tan, B., 2019. PVP-templated highly luminescent copper nanoclusters for sensing trinitrophenol and living cell imaging. Nanoscale 11, 1286–1294. https://doi.org/10.1039/c8nr07142j.

Li, Q., Fernandez-Martinez, A., Lee, B., Waychunas, G.A., Jun, Y.S., 2014. Interfacial energies for heterogeneous nucleation of calcium carbonate on mica and quartz. Environ. Sci. Technol. 48, 5745–5753. https://doi.org/10.1021/es405141j.

Li, Q., Jun, Y.S., 2018. The apparent activation energy and pre-exponential kinetic factor for heterogeneous calcium carbonate nucleation on quartz. Commun. Chem. 1, 1–9. https://doi.org/10.1038/s42004-018-0056-5.

Lillo, C.R., Calienni, M.N., Rivas Aiello, B., Prieto, M.J., Rodriguez Sartori, D., Tuninetti, J., Toledo, P., Alonso, S. del V., Moya, S., Gonzalez, M.C., Montanari, J., Soler-Illia, G.J.A.A., 2020. BSA-capped gold nanoparticles as potential theragnostic for skin diseases: Photoactivation, skin penetration, in vitro, and in vivo toxicity. Mater. Sci. Eng. C 112, 110891. https://doi.org/10.1016/j.msec.2020.110891.

Merabia, S., Shenogin, S., Joly, L., Keblinski, P., Barrat, J.L., 2009. Heat transfer from nanoparticles: A corresponding state analysis. Proc. Natl. Acad. Sci. U. S. A. 106, 15113–15118. https://doi.org/10.1073/pnas.0901372106.

Mérel, P., Tabbal, M., Chaker, M., Moisa, S., Margot, J., 1998. Direct evaluation of the sp 3 content in diamond-like-carbon films by XPS. Appl. Surf. Sci. 136, 105–110. https://doi.org/10.1016/S0169-4332(98)00319-5.

Mishra, G., Bhaskar, T., 2014. Non isothermal model free kinetics for pyrolysis of rice straw. Bioresour. Technol. 169, 614–621. https://doi.org/10.1016/j.biortech.2014.07.045.

Mooij, L., Dam, B., 2013. Nucleation and growth mechanisms of nano magnesium hydride from the hydrogen sorption kinetics. Phys. Chem. Chem. Phys. 15, 11501–11510. https://doi.org/10.1039/c3cp51735g.

Mordike, B.L., Ebert, T., 2001. Magnesium Properties - applications - potential. Mater. Sci. Eng. A 302, 37–45. https://doi.org/10.1016/S0921-5093(00)01351-4.

Nawaz, A., Mishra, R.K., Sabbarwal, S., Kumar, P., 2021. Studies of physicochemical characterization and pyrolysis behavior of low-value waste biomass using Thermogravimetric analyzer: evaluation of kinetic and thermodynamic parameters. Bioresour. Technol. Reports 16,. https://doi.org/10.1016/j.biteb.2021.100858 100858.

Nguyen, T.P., Amgaad, K., Cailler, M., Tran, V.H., Lefrant, S., 1995. XPS analysis of thermal and plasma treated polyparaphenylene-vinylene thin films and their interface formed with aluminum layer. Synth. Met. 69, 495–496. https://doi.org/10.1016/0379-6779(94)02541-6.

Norberto, D.R., Vieira, J.M., de Souza, A.R., Bispo, J.A.C., Bonafe, C.F.S., 2012. Pressure- and Urea-Induced Denaturation of Bovine Serum Albumin: Considerations about Protein Heterogeneity. Open J. Biophys. 02, 4–14. https://doi.org/10.4236/ojbiphy.2012.21002.

Oyelaran, O., Novet, T., Johnson, C.D., Johnson, D.C., 1996. Controlling solid-state reaction pathways: Composition dependence in the nucleation energy of InSe. J. Am. Chem. Soc. 118, 2422–2426. https://doi.org/10.1021/ja953560k.

Palmay, P., Mora, M., Barzallo, D., Bruno, J.C., 2021. Determination of thermodynamic parameters of polylactic acid by thermogravimetry under pyrolysis conditions. Appl. Sci. 11. https://doi.org/10.3390/app112110192.

Patel, A.S., Mohanty, J., 2014. Silver nanoclusters in BSA template: A selective sensor for hydrogen peroxide. J. Mater. Sci. 49, 2136–2143. https://doi.org/10.1007/s10853-013-7906-4.

Ray, S., Bhattacharya, T.K., Singh, V.K., Deb, D., Ghosh, S., Das, S., 2021. Non-isothermal decomposition kinetics of nano-scale CaCO3 as a function of particle size variation. Ceram. Int. 47, 858–864. https://doi.org/10.1016/j.ceramint.2020.08.198.

Sabbarwal, S., Dubey, A.K., Pandey, M., Kumar, M., 2020. Synthesis of biocompatible, BSA capped fluorescent CaCO3pre-nucleation nanoclusters for cell imaging applications. J. Mater. Chem. B 8, 5729–5744. https://doi.org/10.1039/d0tb00881h.

Senum, G.I., Yang, R.T., 1977. Rational approximations of the integral of the Arrhenius function. J. Therm. Anal. 11, 445–447. https://doi.org/10.1007/BF01903696.

Singh, S., Prasad Chakraborty, J., Kumar Mondal, M., 2020. Intrinsic kinetics, thermodynamic parameters and reaction mechanism of non-isothermal degradation of torrefied Acacia nilotica using isoconversional methods. Fuel 259,. https://doi.org/10.1016/j.fuel.2019.116263 116263.

Singh, B., Singh, S., Kumar, P., 2021. In-depth analyses of kinetics, thermodynamics and solid reaction mechanism for pyrolysis of hazardous petroleum sludge based on isoconversional models for its energy potential. Process Saf. Environ. Prot. 146, 85–94. https://doi.org/10.1016/j.psep.2020.08.038.

Starink, M.J., 2003. The determination of activation energy from linear heating rate experiments: A comparison of the accuracy of isoconversion methods. Thermochim. Acta 404, 163–176. https://doi.org/10.1016/S0040-6031(03)00144-8.

Tajima, K., Yamada, Y., Yoshimura, K., 2014. Switchable mirror glass with a Mg-Zr-Ni ternary alloy thin film. Sol. Energy Mater. Sol. Cells 126, 227–236. https://doi.org/10.1016/j.solmat.2013.07.016.

Thomas, J.J., 2007. A new approach to modeling the nucleation and growth kinetics of tricalcium silicate hydration. J. Am. Ceram. Soc. 90, 3282–3288. https://doi.org/10.1111/j.1551-2916.2007.01858.x.

Topală, T., Bodoki, A., Oprean, L., Oprean, R., 2014. Bovine serum albumin interactions with metal complexes. Clujul Med. 87, 5. https://doi.org/10.15386/cjmed-357.

Vyazovkin, S., 1997. Advanced isoconversional method. J. Therm. Anal. 49, 1493–1499. https://doi.org/10.1007/bf01983708.

Vyazovkin, S., 2001. Modification of the Integral Isoconversional Method to Account for Variation in the Activation Energy. J. Comput. Chem. 22, 178–183. https://doi.org/10.1002/1096-987x(20010130)22:2<178::aid-jcc5>3.0.co;2-%23.

Vyazovkin, S., Burnham, A.K., Criado, J.M., Pérez-Maqueda, L.A., Popescu, C., Sbirrazzuoli, N., 2011. ICTAC Kinetics Committee recommendations for performing kinetic computations on thermal analysis data. Thermochim. Acta 520, 1–19. https://doi.org/10.1016/j.tca.2011.03.034.

Wallace, A.F., DeYoreo, J.J., Dove, P.M., 2009. Kinetics of silica nucleation on carboxyl- and amine-terminated surfaces: Insights for biomineralization. J. Am. Chem. Soc. 131, 5244–5250. https://doi.org/10.1021/ja809486b.

Wang, C., Wang, C., Xu, L., Cheng, H., Lin, Q., Zhang, C., 2014. Protein-directed synthesis of pH-responsive red fluorescent copper nanoclusters and their applications in cellular imaging and catalysis. Nanoscale 6, 1775–1781. https://doi.org/10.1039/c3nr04835g.

Wang, F.X., Li, B., 2018. Atomistic calculations of surface and interfacial energies of Mg17Al12-Mg system. Journal of Magnesium and Alloys 6 (4), 375–383. https://doi.org/10.1016/j.jma.2018.08.005.

Wanjun, T., Cunxin, W., Donghua, C., 2006. An investigation of the pyrolysis kinetics of some aliphatic amino acids. J. Anal. Appl. Pyrolysis 75, 49–53. https://doi.org/10.1016/j.jaap.2005.04.003.

Wu, J.B., Chang, J.J., Li, M.Y., Leu, M.S., Li, A.K., 2007. Characterization of diamond-like carbon coatings prepared by pulsed bias cathodic vacuum arc deposition. Thin Solid Films 516, 243–247. https://doi.org/10.1016/j.tsf.2007.06.134.

Yartys, V.A., Lototskyy, M.V., Akiba, E., Albert, R., Antonov, V.E., Ares, J.R., Baricco, M., Bourgeois, N., Buckley, C.E., Bellosta von Colbe, J.M., Crivello, J.C., Cuevas, F., Denys, R.V., Dornheim, M., Felderhoff, M., Grant, D.M., Hauback, B.C., Humphries, T.D., Jacob, I., Jensen, T.R., de Jongh, P.E., Joubert, J.M., Kuzovnikov, M.A., Latroche, M., Paskevicius, M., Pasquini, L., Popilevsky, L., Skripnyuk, V.M., Rabkin, E., Sofianos, M.V., Stuart, A., Walker, G., Wang, H., Webb, C.J., Zhu, M., 2019. Magnesium based materials for hydrogen based energy storage: Past, present and future. Int. J. Hydrogen Energy 44, 7809–7859. https://doi.org/10.1016/j.ijhydene.2018.12.212.

Yin, J., Hu, Y., Yoon, J., 2015. Fluorescent probes and bioimaging: Alkali metals, alkaline earth metals and pH. Chem. Soc. Rev. 44, 4619–4644. https://doi.org/10.1039/c4cs00275j.

Yoshimura, K., Yamada, Y., Okada, M., 2004. Hydrogenation of Pd capped Mg thin films at room temperature. Surf. Sci. 566–568, 751–754. https://doi.org/10.1016/j.susc.2004.06.115.

Yuan, X., He, T., Cao, H., Yuan, Q., 2017. Cattle manure pyrolysis process: Kinetic and thermodynamic analysis with isoconversional methods. Renew. Energy 107, 489–496. https://doi.org/10.1016/j.renene.2017.02.026.

Zabihi, O., Khodabandeh, A., 2013. Understanding of thermal/thermo-oxidative degradation kinetics of polythiophene nanoparticles. J. Therm. Anal. Calorim. 112, 1507–1513. https://doi.org/10.1007/s10973-012-2675-x.

Zhang, C., Jin, J., Zhao, J., Jiang, W., Yin, J., 2013. Functionalized polypropylene non-woven fabric membrane with bovine serum albumin and its hemocompatibility enhancement. Colloids Surfaces B Biointerfaces 102, 45–52. https://doi.org/10.1016/j.colsurfb.2012.08.007.

Zheng, C., Wang, H., Xu, W., Xu, C., Liang, J., Han, H., 2014. Study on the interaction between histidine-capped Au nanoclusters and bovine serum albumin with spectroscopic techniques. Spectrochim. Acta - Part A Mol. Biomol. Spectrosc. 118, 897–902. https://doi.org/10.1016/j.saa.2013.09.082.